

Synergies of Fe Single Atoms and Clusters on N-Doped Carbon Electrocatalyst for pH-Universal Oxygen Reduction

Mengjie Liu, Jeongyeon Lee, Tsung-Cheng Yang, Fangyuan Zheng, Jiong Zhao, Chia-Min Yang,* and Lawrence Yoon Suk Lee*

Single atomic metal–N–C materials have attracted immense interest as promising candidates to replace noble metal-based electrocatalysts for the oxygen reduction reaction (ORR). The coordination environment of metal–N–C active centers plays a critical role in determining their catalytic activity and durability, however, attention is focused only on the coordination of metal atoms. Herein, Fe single atoms and clusters co-embedded in N-doped carbon (Fe/NC) that deliver the synergistic enhancement in pH-universal ORR catalysis via the four-electron pathway are reported. Combining a series of experimental and computational analyses, the geometric and electronic structures of catalytic sites in Fe/NC are revealed and the neighboring Fe clusters are shown to weaken the binding energies of the ORR intermediates on Fe–N sites, hence enhancing both catalytic kinetics and thermodynamics. This strategy provides new insights into the understanding of the mechanism of single atom catalysis.

1. Introduction


The meeting of the increasing energy demand with low carbon emission is one of the major challenges of our times. Oxygen reduction reaction (ORR) is an important rate determining reaction for two promising energy conversion technologies,

M. Liu, Dr. J. Lee, Prof. L. Y. S. Lee
Department of Applied Biology and Chemical Technology
and Research Institute for Smart Energy
The Hong Kong Polytechnic University
Hung Hom, Kowloon, Hong Kong SAR, China
E-mail: lawrence.y.s.lee@polyu.edu.hk

T.-C. Yang, Prof. C.-M. Yang
Department of Chemistry
National Tsing Hua University
Hsinchu 30013, Taiwan
E-mail: cmyang@mx.nthu.edu.tw

F. Zheng, Prof. J. Zhao
Department of Applied Physics
The Hong Kong Polytechnic University
Hung Hom, Kowloon, Hong Kong SAR, China

Prof. C.-M. Yang
Frontier Research Center on Fundamental and Applied Sciences
of Matters
National Tsing Hua University
Hsinchu 30013, Taiwan

 The ORCID identification number(s) for the author(s) of this article can be found under <https://doi.org/10.1002/smt.202001165>.

DOI: 10.1002/smt.202001165

metal air battery and fuel cell. The electrocatalysis of ORR usually requires noble metal catalysts, such as Pt and Pd, to accelerate the reaction in a favorable four-electron pathway.^[1] However, the use of noble metals largely increases the cost of catalytic system; for example, ≈56% of the production cost of proton exchange membrane fuel cell stack is taken up by Pt-based electrocatalysts.^[2] Besides, noble-metal-based electrocatalysts also suffer from methanol and carbon monoxide poisoning during long-term reaction,^[3] making their practical application challenging.

In recent years, various transition metal catalysts, mostly single atoms, embedded in carbon materials have emerged as promising alternatives. These systems offer the advantage of fully utilized atomic

sites with tunable electronic configuration and atomic coordination for good activity and stability over a wide pH range.^[4] Moreover, the surrounding carbon skeletons can be modified with heteroatoms, such as N, P, and S, to stabilize the metal atoms during catalysis, as well as to enhance the overall ORR activity by providing a high specific surface area, good electrical conductivity, and more importantly, tunable d-band center of metal sites.^[5] So far, the single atomic metals on carbon, especially those with M–N–C coordination (M = Fe, Co, Ni, etc.), have demonstrated excellent ORR catalytic activities both experimentally and theoretically.^[4b,6] In addition to the pyrolysis of macrocycles containing M–N₄ coordination, the M–N–C sites can be derived from small nitrogen-carrying precursors (e.g., pyridine and glucosamine) or gaseous NH₃ under appropriate conditions.^[7] Despite the effectiveness of these synthetic strategies, some critical questions concerning the ambiguous configuration of metal sites still remain.

The metal centers coordinated with pyrrolic or pyridinic nitrogen are recognized as well-isolated active sites in the M–N–C materials in most recent reports.^[5a,8] The effect of neighboring metal centers in close proximity, however, has been overlooked, although they would alter the property of the active sites. The possibility of forming clusters or nanoparticles of metals when insufficient nitrogen-containing precursors/ligands are provided could not be excluded, either. The presence of combined atomic sites or even metallic particles has been identified from the “so-called” M–N–C single atom catalysts,^[1,4c,d,7,9] suggesting the possibility of multinuclear sites or clusters acting

as a secondary active site in addition to the single atom sites. These concerted or collaborative active sites that are composed of multiple metal sites are not yet fully understood.

It is often necessary for multiple active sites to cooperate in catalytic processes to adsorb and activate the substrate more efficiently.^[10] The catalytic pathway and thus the resulting activity may differ considerably depending on whether the active site is a single atomic, multiple atomic site, or in other forms. For ORR, the type (single atom or cluster) of metal active centers affect the adsorption model of O₂ molecules (bridge or top-on mode), and thereby determine the catalytic behavior and long-term stability.^[4d,9d] Specifically, it is more favorable for the bridge-*cis* adsorption of O₂ on multiple sites (e.g., single atom-cluster) to undergo the four-electron pathway as O–O bond is stretched for easier breaking, compared with the top-on/side-on adsorption on the single atomic sites.^[4c,11] The presence of another metal atom or cluster in vicinity may also influence the electronic configuration of active metal center. Moreover, the coordination environment of active centers affects the binding strength of O* and OOH* intermediates on metals, and alter the energy barriers of the ORR steps.^[12] Without comprehending how the secondary metal center influences the reaction pathway, the ORR mechanism can be further complicated by the formation of the byproduct H₂O₂, which causes severe activity degradation as a result of electrochemical Fenton reactions (in particular for Fe).^[13] It is thus very important to understand and modulate the coordination environment of active metal sites for enhanced catalytic activity.

Herein, we prepared a Fe single atom/cluster embedded on N-doped carbon (Fe/NC) by the pyrolytic treatment of Fe salts and glucosamine in the presence of porosity-inducing templates. By controlling the composition of reaction mixture, the ratio of different nitrogen species and the atomic-scale dispersion of Fe–N–C active moieties in the porous carbon matrix were simultaneously tuned, which enabled us to study the relationship between the ORR activity and the coordination environment of single atomic/cluster Fe sites. Combining experimental and theoretical investigations, the sites comprising Fe single atoms adjacent to Fe clusters are demonstrated as an excellent pH-universal catalytic centers for ORR with

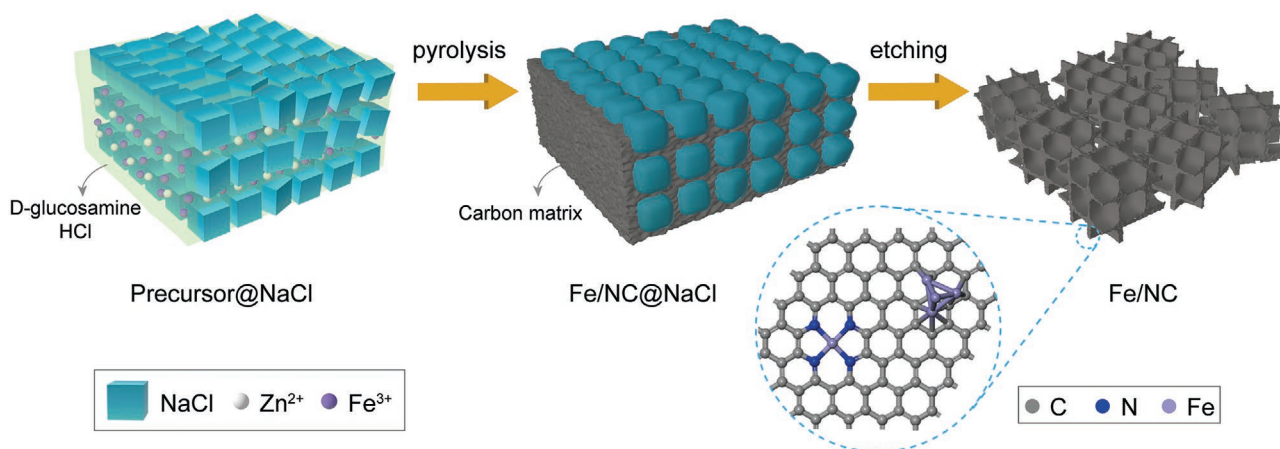
onset potentials of 0.97 and 0.80 V and half-wave potentials of 0.90 and 0.71 V in alkaline and acidic media, respectively.

2. Results and Discussion

2.1. Structural Analysis of Fe/NC Catalysts

Scheme 1 illustrates the synthetic procedure of the Fe/NC catalysts with Fe single atoms/clusters embedded on N-doped carbon. In brief, a mixture of Fe salt, glucosamine, and ZnCl₂ was added to NaCl solution (a hard template). After freeze-drying, the mixture powder was pyrolyzed at 900 °C, followed by rinsing with H₂O and 6 M HCl to remove NaCl and Fe particles. The chelating effect of glucosamine benefits the even distribution of single atomic Fe atoms in the mixture prior to pyrolysis, preventing the aggregation of Fe atoms that may lead to the formation of large Fe particles during the subsequent pyrolysis process. The feeding ratio of NaCl in the reaction mixture was varied (10, 20, and 30 times of the mass of Fe salt), and the obtained Fe/NC catalysts are denoted as Fe/NC-1, Fe/NC-2, and Fe/NC-3, respectively. ZnCl₂ that evaporates during pyrolysis serves as a micropore-inducing agent.^[4b,8a]

The morphology of the as-prepared Fe/NC catalysts was first characterized by scanning electron microscopy (SEM). **Figure 1a** is a typical SEM image of the as-prepared Fe/NC-3, which displays porous honeycomb-like morphology with abundant macropores that range from 0.17 to 0.80 μm (**Figure S1**, Supporting Information). A closer look of the surface of carbon matrix (**Figure 1b**) reveals fine worm-like cracks (average width = 3 nm) over the entire surface, indicating the hierarchical porosity was created by the collegial effect of the NaCl and ZnCl₂. Similar morphologies are observed from Fe/NC-1 and Fe/NC-2 (**Figures S2** and **S3**, Supporting Information). The Brunauer–Emmett–Teller (BET) surface areas of Fe/NC-1, Fe/NC-2, and Fe/NC-3 are measured as 598.4, 641.9, and 773.9 m² g⁻¹, respectively (**Figure 1c**). The Fe/NC-3 shows a higher surface area than the other two owing to the larger quantity of porosity-inducing templates (NaCl and ZnCl₂) used during its synthesis. The pore volume distribution analysis



Scheme 1. Schematic illustration of the synthetic procedures for Fe single atom/nanocluster embedded in N-doped carbon (Fe/NC). The model structure of Fe/NC is shown in the dotted circle.

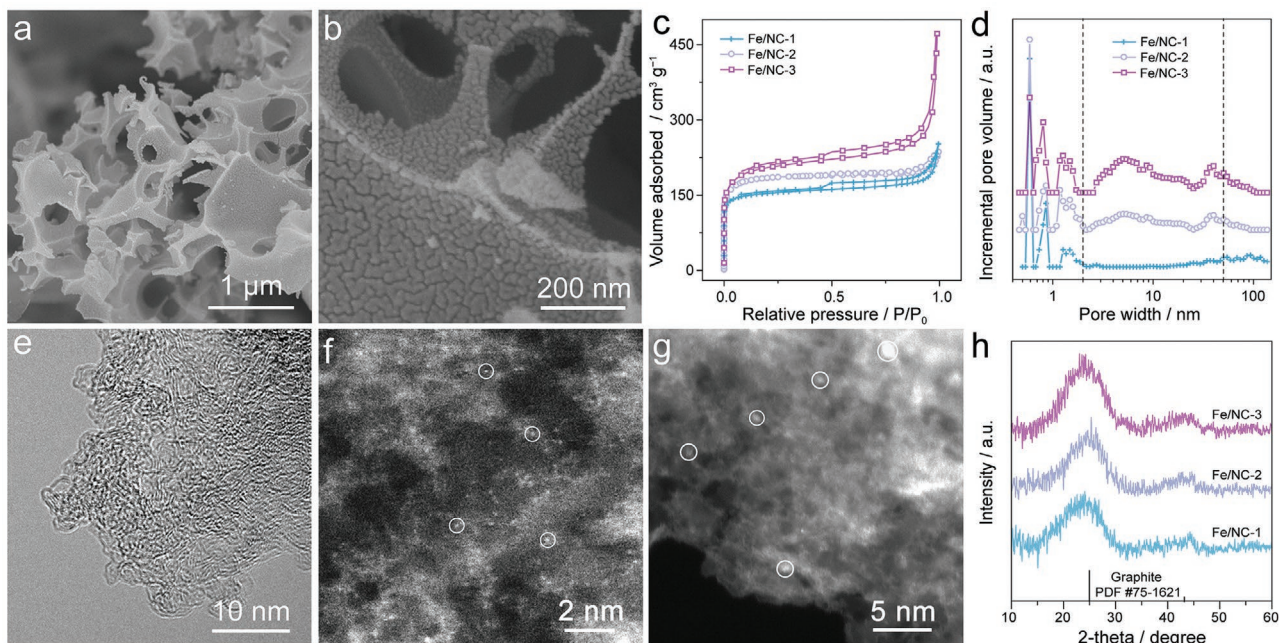


Figure 1. a) Low- and b) high-resolution SEM images of Fe/NC-3. c) N_2 adsorption–desorption isotherms and d) the corresponding pore distribution plots (DFT model) of Fe/NC samples. e) TEM and f–g) HAADF-STEM images of Fe/NC-3. h) Powder XRD patterns of the Fe/NC catalysts.

indicates that Fe/NC-2 and Fe/NC-3 contain micro- and mesopores whose diameters are located at 0.6–2, 5, and 40 nm, while the diameter of pores in Fe/NC-1 is mainly distributed around 0.6–2 and >50 nm. It is evident that the contribution of mesopores (2–50 nm) is influenced by the quantity of NaCl used (Figure 1d).

The transmission electron microscopic (TEM) image of Fe/NC-3 (Figure 1e) displays the graphitic carbon layers stacking with a short-range order. The aberration corrected high-angle annular dark field scanning transmission electron microscopic (HAADF-STEM) image in Figure 1f clearly identifies single Fe atoms that appear as bright dots. In addition to the single atom sites, several bright clusters ($d < 1$ nm) are also visible (Figure 1g; Figure S4, Supporting Information). The elemental mapping by energy dispersive X-ray spectrometry is shown in Figure S5 of the Supporting Information, which unveils the uniform distribution of Fe and N atoms over the entire porous structure. This confirms that Fe single atoms and clusters remained after pyrolysis and acid etching. The Fe/NC-1 and Fe/NC-2 display a similar morphology as Fe/NC-3 but with fewer bright spots (Figure S6, Supporting Information). It has been previously reported that the use of chelating molecules such as glucose can assist the physical isolation of Fe sites, preventing their aggregation during pyrolysis only at mild temperatures (<800 °C).^[6b] The N atom in glucosamine used for the preparation of Fe/NC catalysts provides the chelating effect and preferentially coordinates with Fe to produce single Fe atomic sites. At 900 °C, such protection by chelating agent is inefficient and metallic Fe nanoparticles (but not Fe oxides) are formed due to carbothermal reduction by carbon species generated from glucosamine.^[14] The hemiacetal group at C1 position of glucosamine also plays a role in reducing Fe ions or oxides into metallic Fe.^[15] Hence, the possibility of forming oxide species

such as Fe_2O_3 and Fe_3O_4 can be ruled out. In addition, NaCl acts as a high temperature ionic solvent that offers strong solvation power for reactants and therefore facilitates the Fe nucleation process.^[16] The active Fe atoms, however, are instantly captured by decomposed glucosamine instead of further merging and growing into large particles. As a hard template, NaCl enlarges the surface area of Fe/NC and simultaneously induces the formation of Fe clusters in the carbon matrix.

Powder X-ray diffraction (PXRD) patterns of all Fe/NC catalysts display two broad peaks at 26.2° and 44.3° that correspond to graphite (PDF #75-1621), suggesting their low degree of graphitization (Figure 1h). No other diffraction peaks for metallic Fe or Fe compounds are observed. The Raman spectra of the as-prepared Fe/NC catalysts display two prominent peaks at ≈ 1320 and 1588 cm^{-1} , which can be assigned to the D band (crystal defects) and G band (in-plane stretching of sp^2 C) of carbon species, respectively. The high I_D/I_G ratios (e.g., 1.45 for Fe/NC-3) suggest the disordered and defective nature of carbon matrix (Figure S7, Supporting Information). Such defective carbon matrix possesses the interrupted electronic structure that is known to benefit the boosting of ORR activity.^[17] For instance, the electron-withdrawing feature of highly disordered carbon can lower the electron density of the Fe center that binds oxygen too strongly, and hence optimizes the binding strength of Fe site for the intermediates.^[5b]

The nitrogen species in carbon matrix is favorable for ORR catalysis^[18] and its population on the surface is influenced by the surface area and structure of carbon matrix. X-ray photoelectron spectroscopy (XPS) was employed to investigate the chemical state of nitrogen and other elements on the surface of the as-prepared samples. The survey XPS spectra shown in Figure S8 of the Supporting Information confirm the presence of C, N, O, and Fe elements and no other contaminants

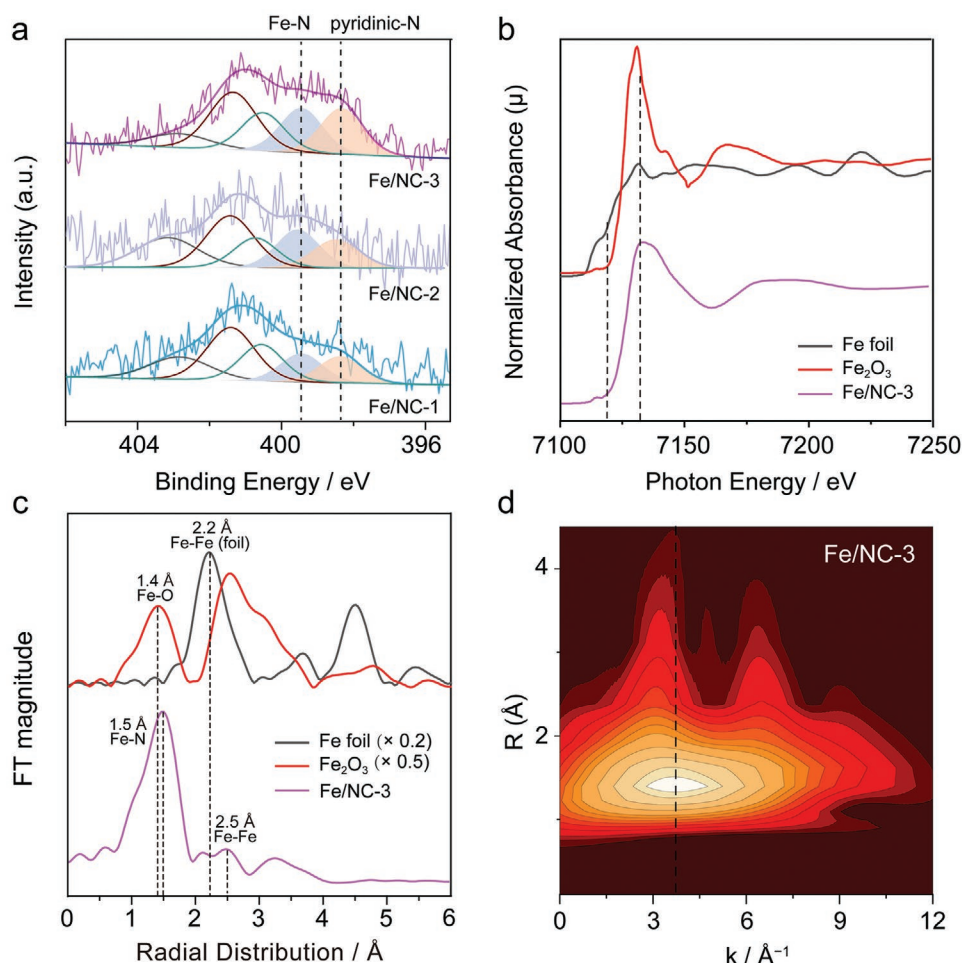


Figure 2. a) High-resolution N 1s XPS spectra of Fe/NC catalysts. b) Normalized Fe K-edge XANES spectra and c) FT profiles of Fe K-edge k^2 -weighted EXAFS data of Fe/NC-3, Fe₂O₃, and Fe foil. d) Wavelet transforms (WT) for EXAFS signals of Fe/NC-3.

are observed. XPS analysis (Table S1, Supporting Information) shows that the surface contents of Fe in the Fe/NC catalysts are ≈ 2.0 wt%, which is consistent with the content (≈ 2.9 wt%) determined by inductively coupled plasma optical emission spectrometry (ICP-OES). All high-resolution N 1s XPS spectra of the Fe/NC catalysts (Figure 2a) can be deconvoluted into five characteristic peaks at 398.3, 399.4, 400.5, 401.3, and 402.8 eV that are assigned to pyridinic N, Fe–N, pyrrolic N, graphitic N, and oxidized N, respectively.^[4b,8a] The Fe–N peak confirms the presence of Fe single atoms anchored on N atoms in the form of Fe–N species. The pyridinic N species at the edges was reported as dominant active sites, which also offered the anchoring site for Fe single atoms.^[19] It is worth noting that the contents of pyridinic N species are greatly enhanced on the Fe/NC-3 surface (21.7%) compared with those on Fe/NC-1 (14.6%) and Fe/NC-2 (15.5%) (Table S2, Supporting Information).

The coordination environment and chemical state of Fe in the Fe/NC catalysts were analyzed by X-ray absorption spectroscopy (XAS). Figure 2b shows the Fe K-edge X-ray absorption near edge structure (XANES) of Fe/NC-3 and two reference samples of Fe₂O₃ and Fe foil. Fe/NC-3 exhibits an absorption edge that is nearly identical to that of Fe₂O₃ but with slightly different

near-edge features, suggesting that the Fe sites in Fe/NC-3 are mainly in +3 oxidation state. Fe/NC-1 and Fe/NC-2 show similar Fe K-edge XANES spectra with Fe/NC-3 (Figure S9a, Supporting Information). The Fourier transform (FT) profiles of Fe K-edge k^2 -weighted extended X-ray absorption fine structure (EXAFS) data in Figure 2c identify the coordination environment of Fe. The major peak at 1.5 Å observed from Fe/NC-3 can be ascribed to the dominant Fe–N(O) scattering path. There is a weak peak at 2.5 Å that corresponds to the Fe–Fe coordination, supporting the existence of relatively small amount of Fe clusters.^[20] The slight difference in R values compared with the Fe–Fe bond of Fe foil (2.2 Å) may be attributed to the different degree of coordination between bulk Fe and Fe clusters. The minor peak related to the Fe clusters is also observed for Fe/NC-1 and Fe/NC-2 (Figure S9b, Supporting Information). The data were fitted and the resulting average coordination numbers (CN) for Fe–N(O) were ≈ 4 for all three samples (Figure S10, see Table S3 of the Supporting Information for fitting results). This implies that the typical FeN₄ moiety is the dominant active center in the Fe/NC catalysts. These coordinatively unsaturated Fe sites are desired for efficient ORR catalysis.^[21] Meanwhile, the CN for Fe–Fe are 0.81, 1.445, and

1.83 for Fe/NC-1, Fe/NC-2, and Fe/NC-3, respectively, indicating the smaller quantity of Fe clusters in the former two. The results of XAS analysis are consistent with the observations of HAADF-STEM. To gain more insights into the k -space resolution, wavelet transform (WT) analysis was conducted and the WT contour plots are presented in Figure 2d. The location of intensity maximum (k , R) is mainly related to the path distance R and atomic number Z .^[6a] From all three samples, one intensity maximum is detected at $\approx 3.8 \text{ \AA}^{-1}$, implying the predominance of Fe–N coordination. Besides, the WT contour plots show an additional peak at high k value ($\approx 7 \text{ \AA}^{-1}$) as an obvious ridge in the 3D plot (Figure S11, Supporting Information) that could be ascribed to Fe–Fe scattering.^[9a]

2.2. Electrocatalytic Performance Analysis of Fe/NC Catalysts

The single atomic Fe–N_x sites and appropriate nitrogen species in porous carbon frameworks render the Fe/NC samples an excellent ORR electrocatalyst. The electrocatalytic activities of the as-prepared samples were evaluated using a rotating ring-disk electrode (RRDE) in both alkaline and acidic electrolytes. Cyclic voltammograms (CVs) were first measured in Ar- and O₂-saturated 1 M KOH to define the onset potential (E_{onset}) where the ORR cathodic peak occurs (Figure S12a, Supporting Information). The Fe/NC-3 affords a high E_{onset} of 0.97 V, which

is close to that of Pt/C (0.98 V), while Fe/NC-1 and Fe/NC-2 display the lower E_{onset} values of 0.92 and 0.93 V, respectively. The electrocatalytic ORR activity of the Fe/NC catalysts was evaluated by linear sweep voltammetry (LSV) in 1 M KOH and compared with that of Pt/C in Figure 3a. Fe/NC-3 achieves an excellent ORR performance with the half-wave potential ($E_{1/2}$) of 0.90 V, which is superior to Pt/C (0.89 V) and surpasses most state-of-the-art non-precious ORR catalysts (Table S5, Supporting Information). Fe/NC-3 also delivers the diffusion-limited current density of $\approx 4.0 \text{ mA cm}^{-2}$, which is comparable to Pt/C. Despite their similar structural features, Fe/NC-1 and Fe/NC-2 exhibit much lower ORR activities than Fe/NC-3 with $E_{1/2}$ values of 0.85 and 0.87 V and diffusion-limited current densities of 3.0 and 2.9 mA cm⁻², respectively. The Tafel slopes obtained from LSV curves are calculated as 123.4, 105.0, and 100.7 mV dec⁻¹ for Fe/NC-1, Fe/NC-2, and Fe/NC-3, respectively (Figure 3b), an indication of the better kinetic process of Fe/NC-3. The similar ORR activity trends are observed in 0.5 M H₂SO₄ and 0.01 M phosphate buffer saline solution (PBS, pH = 7.4), as shown in Figures S13 and S15 of the Supporting Information, respectively. In particular, Fe/CN-3 displays good $E_{1/2}$ values of 0.71 and 0.69 V in acidic and neutral solution, respectively, showing the potential of a pH-universal ORR electrocatalyst. The Nyquist plots obtained by electrochemical impedance spectroscopy (EIS) are compared in Figure S16 of the Supporting Information. The similar semicircles of Fe/NC

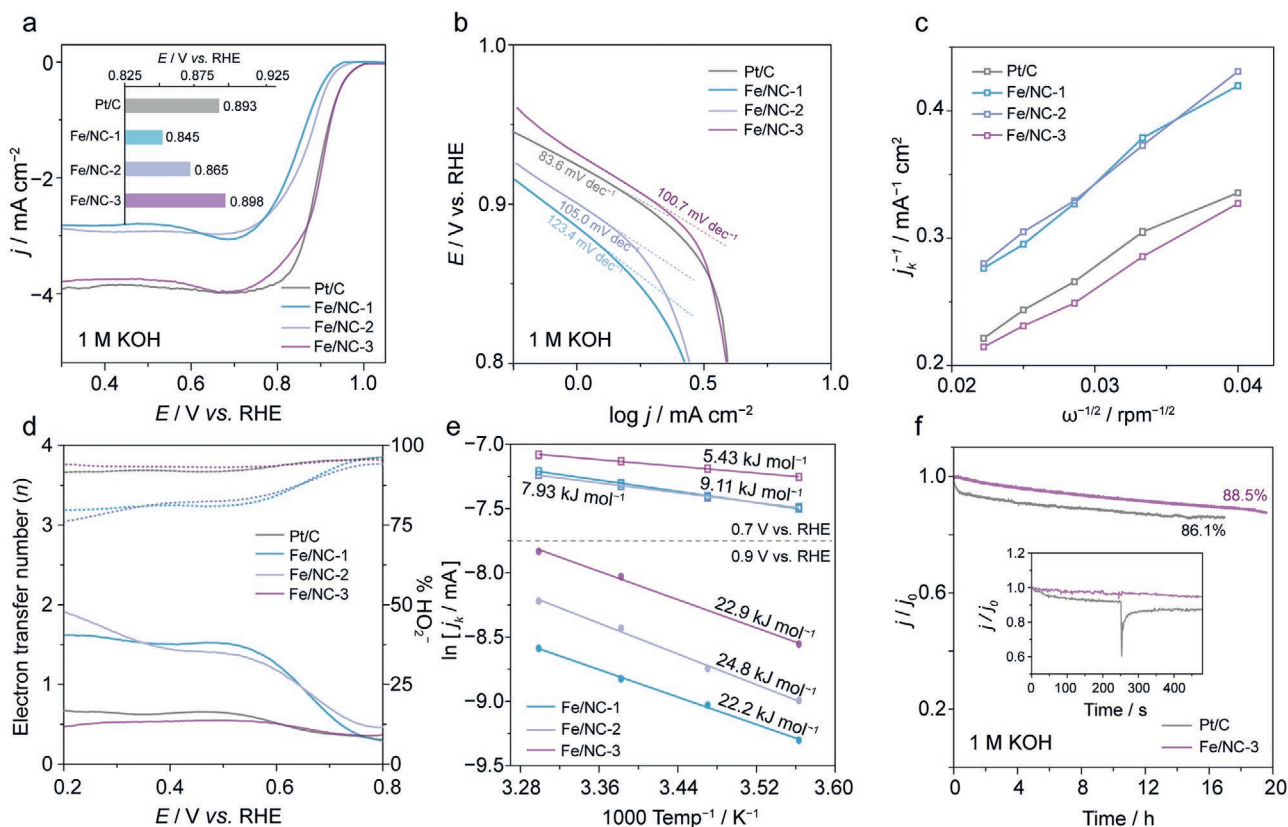


Figure 3. a) ORR polarization curves in O₂-saturated 1 M KOH at 1600 rpm. Inset is the half-wave potentials obtained from the polarization curves. b) The corresponding Tafel plots, and c) the corresponding Kouteck–Levich plots of Fe/NC catalysts and Pt/C. d) Electron transfer number (n) and H₂O₂ yield plotted against applied potential. e) Arrhenius plots of the diffusion-limited current at 0.7 and 0.9 V versus RHE. f) Chronoamperometric responses of Fe/NC-3 and Pt/C in stability test. Inset in (f) is the methanol tolerance test recorded at 0.3 V.

and Pt/C catalysts in high frequency region indicate that they all possess small charge transfer resistance of $\approx 5.4 \Omega$. The large phase angle of Pt/C in mid-frequency region implies the smallest Warburg impedance, as well as the highest diffusion rate. However, in low-frequency region, Fe/NC-3 exhibits a larger phase angle than Pt/C, an indicative of its high accessibility of solvated reactants through the hierarchical pores.

Figure S17 of the Supporting Information presents the LSV curves as-prepared Fe/NC catalysts and Pt/C measured at various rotating speeds. The Kouteck–Levich plots derived from the LSV curves at 0.7 V versus RHE (Figure 3c) display good linear relationship between the reciprocal kinetic current density (j_k^{-1}) and the reciprocal square root of rotating speed ($\omega^{-1/2}$), indicating the first-order ORR reaction kinetics. The electron transfer numbers (n) and peroxide yields (% HO_2^-) of the Fe/NC catalysts are calculated using RRDE polarization curves and compared in Figure 3d. In the potential window of 0.2 and 0.8 V, the n value of Fe/NC-3 remains between 3.75 and 3.85, which is even higher than that of Pt/C (3.63–3.85). By contrast, the n values of Fe/NC-1 and Fe/NC-2 start to drop at 0.74 V and remain at ≈ 3.3 in the potential window of 0.2 and 0.6 V. In the entire potential range, Fe/NC-3 also demonstrates the lowest peroxide production yield of 13.5% compared with the other two Fe/NC catalysts ($>37.7\%$) and Pt/C ($>15.9\%$). These results confirm that the ORR catalytic process at Fe/NC-3 electrode mainly undergoes the four-electron pathway with high selectivity similar to Pt/C, while it is relatively inefficient for the other two Fe/NC catalysts. The high selectivity of Fe/NC-3 seems to be related to the reaction pathway on multiple catalytic sites that inhibit the generation of peroxide byproduct by modulating the energy barriers for intermediates (especially, OOH^*), a phenomenon that will be further discussed in the part on mechanism.

The activation energies (E_a) of the Fe/NC catalysts toward ORR were evaluated at a fixed potential by Arrhenius Equation at temperatures ranging from 285.6 to 303.1 K (Figure S19, Supporting Information). Figure 3e compares the slopes of the Arrhenius plots for Fe/NC catalysts at two applied potentials, one under kinetic control (0.9 V) and the other under kinetic-diffusion mixed control region (0.7 V).^[6c] The corresponding E_a values at 0.9 V are calculated to be 25.9, 24.8, and 22.9 kJ mol^{-1} for Fe/NC-1, Fe/NC-2, and Fe/NC-3, respectively. In the mixed kinetic-diffusion control zone (0.7 V), the Fe/NC samples show a similar trend of E_a values that are decreased by 5 to 10 kJ mol^{-1} . These activation energies are very close to those reported for Pt, such as Pt/C and polycrystalline Pt,^[22] indicating their excellent activities and low energy barriers toward ORR.

Durability is another important criterion for assessing electrocatalytic performance. The durability of Fe/NC-3 was assessed by chronoamperometric response in O_2 -saturated 1 M KOH, as shown in Figure 3f. Fe/NC-3 demonstrates good stability in a 20 h test, showing the retainment of 88.5% of catalytic current, which is slightly better than Pt/C (86.1%). The long-term activity loss most probably results from the demetalation of Fe sites from carbon framework,^[23] as well as the oxidative damage on carbon support by Fenton reaction.^[13b,24] This phenomenon is more serious in acidic medium where the catalytic current is declined by $\approx 22\%$ after a 20 h test (Figure S13c,

Supporting Information). Moreover, unlike Pt/C, the Fe/NC-3 exhibits outstanding tolerances to methanol crossover both in acidic and alkaline solutions, which is beneficial for its practical fuel cell applications (insets in Figure 3f; Figure S13c, Supporting Information).

Based on the results of electrocatalytic experiments, we speculate the high ORR performance of Fe/NC samples stems from their unique structural features, such as the active nitrogen species, the carbon matrix with large surface area, and the synergetic effect of Fe single atom and nanocluster. The Fe/NC catalysts share common Fe–N/Fe–Fe configurations and porous N-doped carbon structure yet the ratio of active nitrogen species present in each catalyst varies. As previously shown in XPS results, Fe/NC-1 and Fe/NC-2 have the lower pyridinic N contents compared with Fe/NC-3. This may be correlated to their ORR activities being inferior to those of Fe/NC-3, suggesting the important role of pyridinic N edge sites in ORR.^[19]

To understand the high ORR activity and synergetic roles of single atomic Fe–N–C moieties and Fe nanoclusters, two poisoning experiments were carried out by adding SCN^- and H_2O_2 to the electrolyte (see Supporting Information for details). SCN^- is known to strongly bind to single atomic Fe–N–C sites, especially under acidic conditions, and thus blocks Fe–N–C sites and lowers ORR activity.^[18,25] On the other hand, Fe clusters are more easily dissolved in peroxide-containing electrolyte, because the protective carbon layers can be damaged by the radicals produced from H_2O_2 in an electrochemical Fenton reaction.^[4a,6b,7] Hence, the ORR contribution from clusters is inhibited, leading to decreased $E_{1/2}$ and current density. Figure 4a–c compares the LSVs of the Fe/NC catalysts before and after the addition of $10 \times 10^{-3} \text{ M SCN}^-$. The ORR performance of Fe/NC-3 obviously declines with the reduction of $E_{1/2}$ value by $\approx 170 \text{ mV}$. The ORR activities also diminish in the cases of Fe/NC-1 and Fe/NC-2 as manifested by the dropping of their $E_{1/2}$ values by 195 and 180 mV, respectively. The opposite trend of ORR performance decline is seen in the Fe/NC samples of the H_2O_2 poisoning tests (Figure 4d–f). The high ring currents (black dashed line) indicate that the added H_2O_2 is detected by the Pt ring electrode in all three samples. However, the shift of $E_{1/2}$ only occurs in Fe/NC-3 ($\approx 100 \text{ mV}$), but is negligible in the other catalysts, which suggests the Fe nanocluster population is significant in Fe/NC-3. However, it is still unclear whether the activity degradation is directly caused by the absence of Fe nanoclusters or the broken synergetic role between SA sites and clusters.

2.3. Density Functional Theory (DFT) Calculation

Since both Fe single atoms and nanoclusters were experimentally confirmed to benefit the ORR catalysis, we further carried out DFT calculations to gain insights into the binding energies of reactants and the corresponding energy barriers. Three ideal models representing Fe single atom (FeN_4/C), nanocluster (Fe_4/C , atom number was set as four according to the STEM and EXAFS results), and single atom/nanocluster hybrid ($\text{FeN}_4/\text{Fe}_4/\text{C}$) on carbon skeleton are proposed in the calculation. For the pure cluster model, Fe_4 surface is the active site; for the other two models, the single atomic Fe is regarded as the main

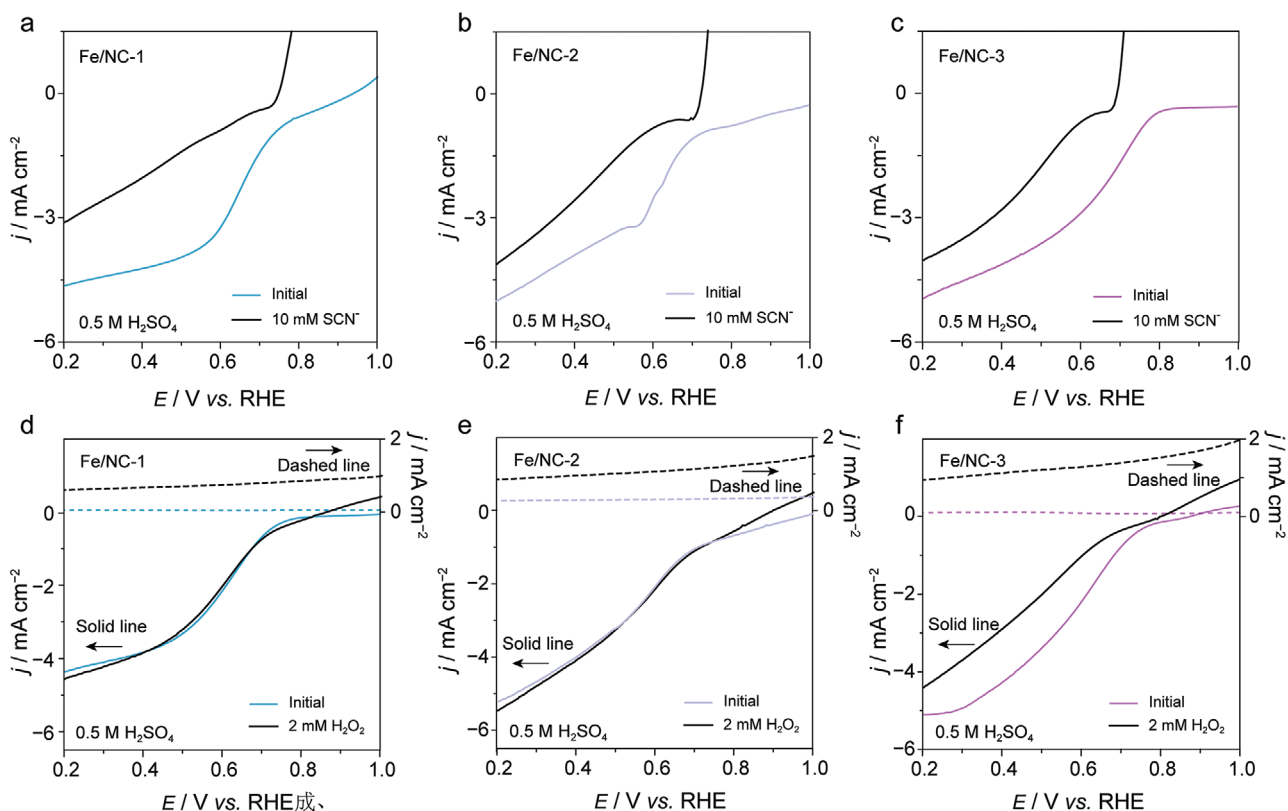


Figure 4. SCN^- poisoning experiments represented by LSV curves in 0.5 M H_2SO_4 for a) Fe/NC-1, b) Fe/NC-2, and c) Fe/NC-3. H_2O_2 poisoning experiments represented by RRDE polarization curves in 0.5 M H_2SO_4 for d) Fe/NC-1, e) Fe/NC-2, and f) Fe/NC-3.

ORR catalytic center, while the adjacent Fe nanoclusters on the carbon matrix do not directly participate in the catalytic process, but serve as an electron donor to carbon layer. Therefore, an associative pathway on singular Fe site is taken into consideration in this case.

The d-band center of Fe single atom is related to Fermi level and its electron occupation can influence the binding strength between intermediates and catalytic surface.^[4d,26] The projected density of states (PDOS) for d orbitals is displayed in Figure 5a and Figure S25 (Supporting Information). The d-band center of Fe in $\text{FeN}_4/\text{Fe}_4/\text{C}$ (-2.72 eV) is shifted negatively compared to those in single atom (FeN_4/C , -2.62 eV) and cluster sites (Fe_4/C , -2.19 eV). The different d-band center values can be attributed to the influence of nearby Fe nanocluster, as mentioned before. Metallic Fe can provide electron to carbon matrix, then pull up the Fermi level of the whole system and downshift its d-band center. Therefore, the interaction strength between reactants and metal center decreases in the $\text{FeN}_4/\text{Fe}_4/\text{C}$ hybrid with the deepest d-band center, endowing it with an optimized free energy. To validate the result, the Gibbs free energy diagram for $\text{FeN}_4/\text{Fe}_4/\text{C}$ at 1.23 V is compared with others in Figure 5b and Figure S26 (Supporting Information). Both the first and fourth elementary steps are thermodynamically unfavorable, as indicated by the large energy uphill. For the FeN_4/C model, 0.57 eV is required for the potential determining step ($\text{HO}^* + \text{H} + \text{e}^- \rightarrow \text{H}_2\text{O} + ^*$), while the value is decreased to 0.5 eV for $\text{FeN}_4/\text{Fe}_4/\text{C}$, which results in a faster ORR kinetics and a lower energy barrier. Based on these

calculation results, the ORR mechanism on $\text{FeN}_4/\text{Fe}_4/\text{C}$ in base is proposed as illustrated in Figure 5c.

3. Conclusion

In summary, Fe single atoms coembedded with Fe clusters on N-doped carbon have been prepared with the control of cluster population and N site type. The monodispersed single atomic sites, unique single atom/cluster structure, and the pyridinic-N-rich carbon framework of hierarchical porosity contribute to the ORR activity and stability in both alkaline and acidic media, as manifested by the high E_{onset} of 0.97 V in base and 0.80 V in acid. DFT calculations verify that the excellent ORR performance stems from the deepened d-band center and weakened binding strength for intermediates. This study provides insights into the optimal active centers in single atomic catalytic systems as well as a synthetic guidance for Fe-based ORR catalyst design.

4. Experimental Section

Chemicals: D-Glucosamine hydrochloride, zinc chloride (ZnCl_2 , $\geq 98\%$), iron(III) chloride (FeCl_3 , 97%), and potassium hydroxide (KOH, 99.99%) were purchased from Sigma-Aldrich. Sodium chloride (NaCl , $\geq 99\%$) was obtained from J&K Chemical. All chemicals were directly used without any purification.

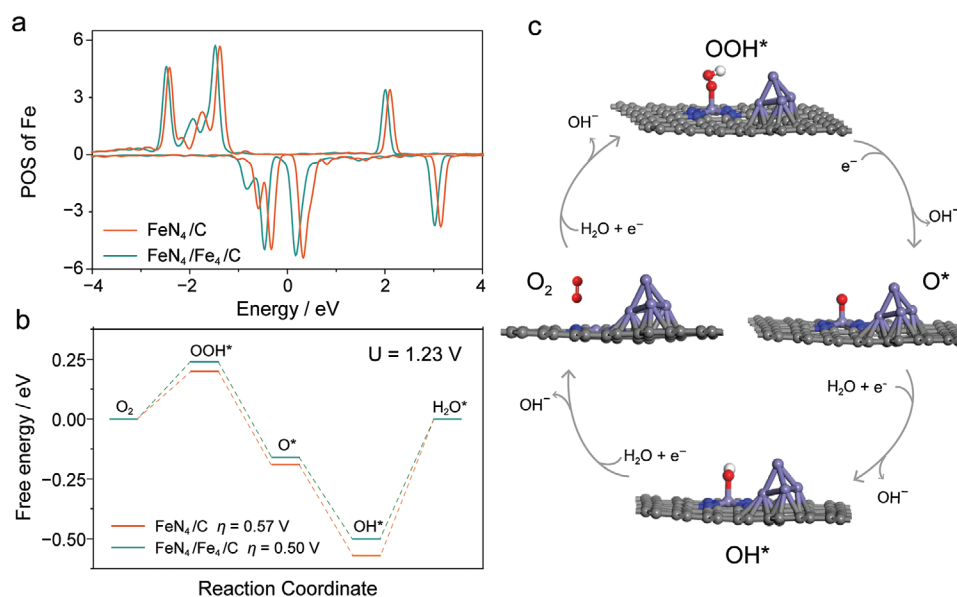


Figure 5. a) PDOS of modelling structure of FeN₄/C and FeN₄/Fe₄/C, b) the corresponding free energy diagrams for ORR at U = 1.23 V, pH = 0, and c) proposed ORR mechanism in alkaline solution of FeN₄/Fe₄/C structure. White, red, gray, blue, and purple balls represent H, O, C, N, and Fe atoms, respectively.

Preparation of Fe/NC Electrocatalysts: NaCl (2, 4, or 6 g) was dissolved in deionized Milli-Q water (30 mL, >18 MΩ). To this solution, D-glucosamine hydrochloride (1.6 g), ZnCl₂ (0.21 g), and FeCl₃ (0.19 g) were added and sonicated for 1 h. After freeze-drying, the obtained powder was heated at 900 °C for 5 h with a heating rate of 5 °C min⁻¹ under nitrogen flow of 100 sccm. The annealed powder was dispersed in DI water at 90 °C for 24 h to completely remove NaCl, followed by etching with 6 M HCl. The as-prepared samples were freeze-dried again and denoted as Fe/NC-1, Fe/NC-2, and Fe/NC-3 according to the NaCl-to-FeCl₃ mass ratio of 10, 20, and 30, respectively.

Physical Characterization: The morphology of samples was characterized using a field emission scanning electron microscope (TESCAN MAIA3) and a transmission electron microscope (JEOL Model JEM-2100F, 200 kV) equipped with an energy dispersive X-ray spectrometer for elemental composition analysis and distribution mappings. The aberration corrected HAADF images were taken by an STEM JEM-ARM200F (13 μA, 60 kV) equipped with a CEOS spherical aberration corrector. During the measurement, the vacuum level was kept at 1.3 × 10⁻⁷ mbar. The size of the scanning probe was ≈1.5 Å. With a defocus of -4 nm, the acquisition time of HAADF images was set to 19 μs per pixel to minimize damage and obtain graphics with lower drift. Images of 512 × 512 pixels were obtained with a camera length aperture of 40 μm, and the collection angles ranging from 45 to 180 mrad were used to obtain atomic images with appropriate contrast. Wiener filtering was applied to HAADF images to reduce noise. PXRD patterns were collected on a SmartLab X-ray diffractometer (200 mA, 45 kV) by Rigaku. XPS spectra were acquired by a K-Alpha XPS system (Thermo Fisher Scientific, Al Kα, hν = 1486.8 eV). The C 1s peak at 284.6 eV was used for spectrometer calibration. The data were analyzed using CasaXPS software, with a background type of Shirley and peak profile of Gaussian-Lorentzian GL(30). A Raman spectrometer (inVia confocal Renishaw Micro-Raman Spectroscopy Systems) with 785 nm stream-line laser excitation was used for the ex situ Raman spectroscopic study. The surface area analysis was conducted on a Micromeritics ASAP 2020 Plus Physisorption analyzer using N₂. The elemental composition was determined by ICP-OES on an Agilent 710 Series spectrometer by three independent experiments. The digestion solution was prepared by leaching Fe/NC samples in aqua regia at 60 °C overnight.

The Fe K-edge XAS measurements were carried out at beamline 17 C in National Synchrotron Radiation Research Center (NSRRC),

Taiwan. The powdered samples of Fe/NC were pressed into a self-supporting disk before being mounted on a sample holder for measurements. Fe foil was measured simultaneously as a reference sample for energy calibration. For a measured spectrum, the EXAFS function χ was obtained by subtracting the postedge background from the initial spectrum and then normalizing to the edge jump step. The energy space of the normalized $\chi(E)$ was then transformed into the k space of $\chi(k)$. The $\chi(k)$ was multiplied by k^2 to compensate for the oscillation dampening in the high- k region, and the k^2 -weighted $\chi(k)$ data in the range of 2.5–10.7 Å⁻¹ were converted to the R -space data by the FT. Athena software was used to process the XAS data, including background subtraction, normalization of edge jump step, and FT of the k^2 -weighted $\chi(k)$ data. Artemis software was applied to fit the FT profiles.

Electrochemical Measurements: All the electrochemical measurements were conducted in a three-electrode cell on an electrochemical potentiostat (PINE Wavedriver) at 25 °C. The Hg/HgO and Ag/AgCl (saturated KCl solution) electrodes served as the reference electrodes in alkaline, neutral, and acidic environments using Ar- or O₂-saturated 1 M KOH, 0.01 M PBS (pH = 7.4), and 0.5 M H₂SO₄ as electrolytes, respectively. Pt foil was used as the counter electrode. An RRDE with a glassy carbon disk (0.2475 cm²) and a Pt ring served as the bare working electrode. All the potentials were referred to the RHE as follows

$$E(\text{vs RHE}) = E(\text{vs Ag/AgCl}) + 0.197 + 0.059 \text{ pH} \quad (1)$$

$$E(\text{vs RHE}) = E(\text{vs Hg/HgO}) + 0.098 + 0.059 \text{ pH} \quad (2)$$

For catalyst preparation, typically, 5 mg of sample was dispersed by sonication in a mixed solution containing DI water (0.5 mL), ethanol (0.5 mL), and 5 wt% Nafion (20 μL). A control sample was prepared using commercial Pt/C (20 wt%, Sigma-Aldrich) by the same method to form 5 mg mL⁻¹ catalyst ink. 15 μL of catalyst ink was loaded on an RRDE for test, making the final loading amount of catalyst to be 0.3 mg cm⁻². CVs and LSVs were recorded at scan rates of 50 and 5 mV s⁻¹, respectively. Before measuring each LSV curve, 10 cycles of CVs were swept to stabilize the catalysts. The double-layer capacitive currents measured in the Ar-saturated electrolyte were deducted from the polarization curves. Electrochemical impedance spectra (EIS) were collected at 0.7 V versus RHE in O₂-saturated 1 M KOH in the frequency range from 100 k to 0.1 Hz with an amplitude of 5 mV.

The K–L plots were obtained by plotting the reciprocal current density (j^{-1}) versus the reciprocal square root of rotating speeds ($\omega^{-1/2}$) based on the measurements at different rotation speeds ranging from 400 to 2500 rpm. The kinetic current density can be calculated according to the following K–L equation

$$\frac{1}{j} = \frac{1}{j_L} + \frac{1}{j_K} = \frac{1}{B\omega^{1/2}} + \frac{1}{j_K} \quad (3)$$

$$B = 0.2nFC_O D^{2/3} \nu^{-1/6} \quad (4)$$

where j is the measured current density, j_K and j_L are the kinetic and diffusion-limited current densities, B is the slope of K–L plot, ω is the linear rotation speed expressed in rpm, F is the Faradaic constant (96 485.3 C mol⁻¹), C_O is the concentration of oxygen (1.2 × 10⁻⁶ mol cm⁻³), D is the diffusion coefficient of oxygen (1.9 × 10⁻⁵ cm² s⁻¹ in 1 M KOH and in 0.5 M H₂SO₄), and ν is the kinematic viscosity of the electrolyte (1.13 × 10⁻² cm² s⁻¹).

The electron transfer number (n) and peroxide yield (% HO₂⁻) were determined as follows

$$n = 4 \times \frac{I_d}{I_d + I_r/N} \quad (5)$$

$$\%HO_2^- = 200 \times \frac{I_r/N}{I_d + I_r/N} \quad (6)$$

where I_d is the disk current, I_r is the ring current, and N is the current collection efficiency of the Pt ring (37%).

Arrhenius plots were obtained by plotting the catalytic currents against the reciprocal of temperatures. A sealed cell was used to minimize the evaporative loss of electrolyte solution. The temperature of solution was controlled by thermostatic water bath. The dependence of catalytic currents on the temperature is shown in Figure S19 of the Supporting Information. According to the Arrhenius relationship

$$k = A \exp\left(\frac{-E_a}{RT}\right) \quad (7)$$

where k is the rate constant, A is pre-exponential factor, R is the universal gas constant (8.314 J mol⁻¹ K⁻¹), and T is the temperature. The apparent electrochemical activation enthalpy E_a for OER can be determined by the slope of Arrhenius plot

$$\frac{\partial(\ln i_0)}{\partial(1/T)} = -\frac{E_a}{R} \quad (8)$$

where i_0 is the kinetic current density.

For SCN⁻ poisoning experiment, 1 mL of 1 M KSCN solution was added to 100 mL of O₂-saturated 0.5 M H₂SO₄, and LSV curve was immediately collected. For H₂O₂ poisoning test, 20 μL of 30% H₂O₂ solution was added to fresh electrolyte, and the catalyst-coated electrode was scanned from 1.1 to 0.5 V for 20 cycles to poison the iron clusters. Then, RRDE polarization curves were obtained at a scan rate of 5 mV s⁻¹. Pt ring electrode was used to collect the current signal of added H₂O₂.

Computational Calculations: In this work, the spin-polarized plane wave DFT was performed using the Vienna ab initio simulation package. The atomic structure of the catalyst systems was constructed based on experimental results. The ion–electron interaction was treated by the projector augmented wave method. Electron exchange–correlation was represented by the functional of Perdew, Burke, and Ernzerhof of generalized gradient approximation. The cutoff energy for plane-wave basis was set to 500 eV. Periodic boundary conditions with a vacuum space 15 Å were applied to avoid the interaction between the neighboring periodic structures. The convergence tolerance was 10⁻⁵ eV and 0.01 eV Å⁻¹ for energy and force, respectively. DFT–D3 calculations were used to describe the van der Waals interaction. The k -points were generated automatically using the Monkhorste–Pack method, with

a k -point mesh of 3 × 3 × 1 for the structure relaxation and electronic property calculations.

The ORR performance was characterized by the reaction free energy of the adsorbed intermediate (OOH, O, OH), defined as

$$\Delta G = \Delta E + \Delta ZPE - T\Delta S \quad (9)$$

where ΔG , ΔE , ΔZPE , and $T\Delta S$ are the change of the free energy, total energy from DFT calculations, zero-point energy, and entropic contributions (T was set to be 300 K), respectively. The zero-point energy can be obtained from vibrational frequencies derived from Hessians calculation from analytic gradients on single molecule in vacuum or adsorbates. The TS values of molecular O₂, H₂O, and H₂ were taken from the previous report.

Supporting Information

Supporting Information is available from the Wiley Online Library or from the author.

Acknowledgements

M.L. and J.L. contributed equally to this work. The authors gratefully acknowledge the financial supports from the Innovation and Technology Commission of Hong Kong and the Hong Kong Polytechnic University (1-BE0Y and Q-CDA3), the Ministry of Science and Technology, Taiwan (MOST 109-2113-M-007-018-MY3 and MOST 109-2634-F-007-023), as well as the supports from the Frontier Research Center on Fundamental and Applied Sciences of Matters from The Featured Areas Research Center Program within the framework of the Higher Education Sprout Project by the Ministry of Education (MOE) in Taiwan. National Synchrotron Radiation Research Centre (NSRRC), Taiwan is gratefully acknowledged for XAS measurements.

Conflict of Interest

The authors declare no conflict of interest.

Data Availability Statement

Research data are not shared.

Keywords

Fe clusters, Fe–N–C, oxygen reduction reaction, porous carbon, single atom catalysis

Received: November 25, 2020

Revised: January 23, 2021

Published online:

- [1] A. Zitolo, V. Goellner, V. Armel, M.-T. Sougrati, T. Mineva, L. Stievano, E. Fonda, F. Jaouen, *Nat. Mater.* **2015**, *14*, 937.
- [2] a) Y. Nie, L. Li, Z. Wei, *Chem. Soc. Rev.* **2015**, *44*, 2168; b) W. Wang, Q. Jia, S. Mukerjee, S. Chen, *ACS Catal.* **2019**, *9*, 10126.
- [3] X. Cheng, Z. Shi, N. Glass, L. Zhang, J. Zhang, D. Song, Z.-S. Liu, H. Wang, J. Shen, *J. Power Sources* **2007**, *165*, 739.
- [4] a) C. H. Choi, C. Baldizzone, J.-P. Grote, A. K. Schuppert, F. Jaouen, K. J. J. Mayrhofer, *Angew. Chem., Int. Ed.* **2015**, *54*, 12753; b) C. Zhu,

- Q. Shi, B. Z. Xu, S. Fu, G. Wan, C. Yang, S. Yao, J. Song, H. Zhou, D. Du, S. P. Beckman, D. Su, Y. Lin, *Adv. Energy Mater.* **2018**, *8*, 1801956; c) Z. Lu, B. Wang, Y. Hu, W. Liu, Y. Zhao, R. Yang, Z. Li, J. Luo, B. Chi, Z. Jiang, M. Li, S. Mu, S. Liao, J. Zhang, X. Sun, *Angew. Chem., Int. Ed.* **2019**, *58*, 2622; d) M. Xiao, Y. Chen, J. Zhu, H. Zhang, X. Zhao, L. Gao, X. Wang, J. Zhao, J. Ge, Z. Jiang, S. Chen, C. Liu, W. Xing, *J. Am. Chem. Soc.* **2019**, *141*, 17763.
- [5] a) M. Xiao, L. Gao, Y. Wang, X. Wang, J. Zhu, Z. Jin, C. Liu, H. Chen, G. Li, J. Ge, Q. He, Z. Wu, Z. Chen, W. Xing, *J. Am. Chem. Soc.* **2019**, *141*, 19800; b) N. Ramaswamy, U. Tylus, Q. Jia, S. Mukerjee, *J. Am. Chem. Soc.* **2013**, *135*, 15443.
- [6] a) H. Fei, J. Dong, M. J. Arellano-Jiménez, G. Ye, N. Dong Kim, E. L. G. Samuel, Z. Peng, Z. Zhu, F. Qin, J. Bao, M. J. Yacaman, P. M. Ajayan, D. Chen, J. M. Tour, *Nat. Commun.* **2015**, *6*, 8668; b) L. Zhao, Y. Zhang, L.-B. Huang, X.-Z. Liu, Q.-H. Zhang, C. He, Z.-Y. Wu, L.-J. Zhang, J. Wu, W. Yang, L. Gu, J.-S. Hu, L.-J. Wan, *Nat. Commun.* **2019**, *10*, 1278; c) L. Osmieri, A. H. A. Monteverde Videla, P. Ocón, S. Specchia, *J. Phys. Chem. C* **2017**, *121*, 17796; d) Z. Zhu, H. Yin, Y. Wang, C.-H. Chuang, L. Xing, M. Dong, Y.-R. Lu, G. Casillas-Garcia, Y. Zheng, S. Chen, Y. Dou, P. Liu, Q. Cheng, H. Zhao, *Adv. Mater.* **2020**, *32*, 2004670.
- [7] U. Tylus, Q. Jia, K. Strickland, N. Ramaswamy, A. Serov, P. Atanassov, S. Mukerjee, *J. Phys. Chem. C* **2014**, *118*, 8999.
- [8] a) H. Zhang, S. Hwang, M. Wang, Z. Feng, S. Karakalos, L. Luo, Z. Qiao, X. Xie, C. Wang, D. Su, Y. Shao, G. Wu, *J. Am. Chem. Soc.* **2017**, *139*, 14143; b) X. Wan, X. Liu, Y. Li, R. Yu, L. Zheng, W. Yan, H. Wang, M. Xu, J. Shui, *Nat. Catal.* **2019**, *2*, 259.
- [9] a) S. Ji, Y. Chen, Q. Fu, Y. Chen, J. Dong, W. Chen, Z. Li, Y. Wang, L. Gu, W. He, C. Chen, Q. Peng, Y. Huang, X. Duan, D. Wang, C. Draxl, Y. Li, *J. Am. Chem. Soc.* **2017**, *139*, 9795; b) H. Li, K. Du, C. Xiang, P. An, X. Shu, Y. Dang, C. Wu, J. Wang, W. Du, J. Zhang, S. Li, H. Tian, S. Wang, H. Xia, *J. Mater. Chem. A* **2020**, *8*, 17136; c) Y. Lei, F. Yang, H. Xie, Y. Lei, X. Liu, Y. Si, H. Wang, *J. Mater. Chem. A* **2020**, *8*, 20629; d) N. Zhang, T. Zhou, J. Ge, Y. Lin, Z. Du, C. a. Zhong, W. Wang, Q. Jiao, R. Yuan, Y. Tian, W. Chu, C. Wu, Y. Xie, *Matter* **2020**, *3*, 509.
- [10] a) C. Dong, Y. Li, D. Cheng, M. Zhang, J. Liu, Y.-G. Wang, D. Xiao, D. Ma, *ACS Catal.* **2020**, *10*, 11011; b) E. Guan, J. Ciston, S. R. Bare, R. C. Runnebaum, A. Katz, A. Kulkarni, C. X. Kronawitter, B. C. Gates, *ACS Catal.* **2020**, *10*, 9065.
- [11] E. Yeager, *J. Mol. Catal.* **1986**, *38*, 5.
- [12] X. Guo, S. Lin, J. Gu, S. Zhang, Z. Chen, S. Huang, *ACS Catal.* **2019**, *9*, 11042.
- [13] a) C. H. Choi, H.-K. Lim, M. W. Chung, G. Chon, N. Ranjbar Sahraie, A. Altin, M.-T. Sougrati, L. Stievano, H. S. Oh, E. S. Park, F. Luo, P. Strasser, G. Dražić, K. J. J. Mayrhofer, H. Kim, F. Jaouen, *Energy Environ. Sci.* **2018**, *11*, 3176; b) H. Singh, S. Zhuang, B. Ings, B. B. Nunna, E. S. Lee, *Carbon* **2019**, *151*, 160.
- [14] a) S. T. Neeli, H. Ramsurn, *Carbon* **2018**, *134*, 480; b) Y. Shen, *J. Mater. Chem. A* **2015**, *3*, 13114.
- [15] a) P. Raveendran, J. Fu, S. L. Wallen, *Green Chem.* **2006**, *8*, 34; b) N. N. Mallikarjuna, R. S. Varma, *Cryst. Growth Des.* **2007**, *7*, 686.
- [16] a) X. Liu, N. Fechler, M. Antonietti, *Chem. Soc. Rev.* **2013**, *42*, 8237; b) K. V. Manukyan, K. G. Kirakosyan, Y. G. Grigoryan, O. M. Niazyan, A. V. Yeghishyan, A. G. Kirakosyan, S. L. Kharatyan, *Ind. Eng. Chem. Res.* **2011**, *50*, 10982.
- [17] a) Y. Jiang, L. Yang, T. Sun, J. Zhao, Z. Lyu, O. Zhuo, X. Wang, Q. Wu, J. Ma, Z. Hu, *ACS Catal.* **2015**, *5*, 6707; b) X. Yan, Y. Jia, X. Yao, *Chem. Soc. Rev.* **2018**, *47*, 7628.
- [18] J. Masa, W. Xia, M. Muhler, W. Schuhmann, *Angew. Chem., Int. Ed.* **2015**, *54*, 10102.
- [19] a) E. Luo, M. Xiao, J. Ge, C. Liu, W. Xing, *J. Mater. Chem. A* **2017**, *5*, 21709; b) J. Luo, K. Wang, X. Hua, W. Wang, J. Li, S. Zhang, S. Chen, *Small* **2019**, *15*, 1805325; c) L. Lai, J. R. Potts, D. Zhan, L. Wang, C. K. Poh, C. Tang, H. Gong, Z. Shen, J. Lin, R. S. Ruoff, *Energy Environ. Sci.* **2012**, *5*, 7936.
- [20] L. Liu, X. Zhao, R. Li, H. Su, H. Zhang, Q. Liu, *ACS Appl. Mater. Interfaces* **2019**, *11*, 41432.
- [21] Z. Zhang, J. Sun, F. Wang, L. Dai, *Angew. Chem., Int. Ed.* **2018**, *57*, 9038.
- [22] a) A. B. Anderson, J. Roques, S. Mukerjee, V. S. Murthi, N. M. Markovic, V. Stamenkovic, *J. Phys. Chem. B* **2005**, *109*, 1198; b) U. A. Paulus, T. J. Schmidt, H. A. Gasteiger, R. J. Behm, *J. Electroanal. Chem.* **2001**, *495*, 134.
- [23] C. H. Choi, C. Baldizzone, G. Polymeros, E. Pizzutilo, O. Kasian, A. K. Schuppert, N. Ranjbar Sahraie, M.-T. Sougrati, K. J. J. Mayrhofer, F. Jaouen, *ACS Catal.* **2016**, *6*, 3136.
- [24] V. Goellner, C. Baldizzone, A. Schuppert, M. T. Sougrati, K. Mayrhofer, F. Jaouen, *Phys. Chem. Chem. Phys.* **2014**, *16*, 18454.
- [25] X. Yang, D. Xia, Y. Kang, H. Du, F. Kang, L. Gan, J. Li, *Adv. Sci.* **2020**, *7*, 2000176.
- [26] G. Gao, E. R. Waclawik, A. Du, *J. Catal.* **2017**, *352*, 579.